ACS OMEGA

http://pubs.acs.org/journal/acsodf

Article

Electronic Structures and Electrical Properties of Cr^{2+}-, Cu^{2+}-, Ni^{2+}-, and Zn^{2+}-Doped Sodium Titanate Nanotubes

Hager Samir, Mohamed Taha, S.I. El-Dek, and Ayman H. Zaki*

Cite This: *ACS Omega* 2022, 7, 27587−27601

Read Online

ACCESS | Metrics & More | Article Recommendations

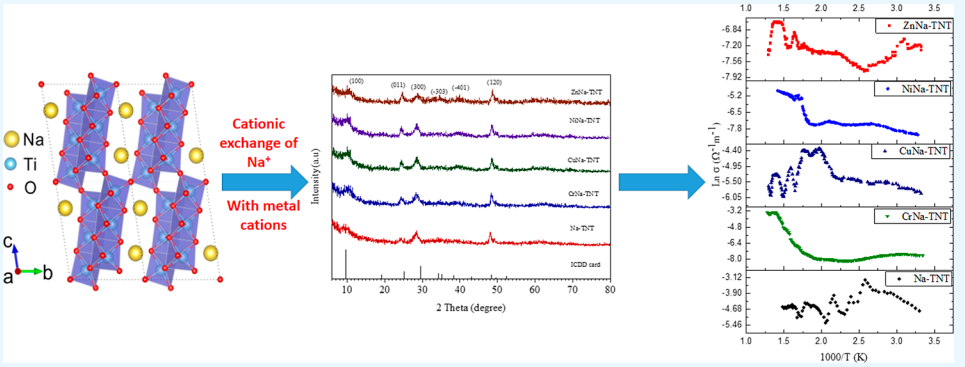

ABSTRACT: Sodium titanate nanotubes (Na-TNTs) and their metal-doped derivatives were prepared using simple hydrothermal and metal ion-exchange methods, respectively. The as-prepared doped materials were characterized by X-ray powder diffraction, thermal gravimetric analysis, high-resolution transmission electron microscopy, field-emission scanning electron microscopy, and energy-dispersive X-ray spectroscopy. The dielectric constant, the loss tangent, and the AC electrical conductivity of NaM-TNTs (where M = Cr, Cu, Ni, or Zn) were measured at selected frequencies (400 kHz and 2 MHz) as a function of temperature. The activation energy was calculated and reported at 400 kHz. All samples showed mixed ionic electronic conductivity. Some of the materials were used as examples for theoretically exploring structures and optoelectronic properties (density of states, reflectivity, absorption curve, refractive index, dielectric function, optical conductivity, and loss function) using density functional theory calculations. The band gaps of the materials were found to vary from 2.4 to 3.17 eV, which makes them suitable for many optoelectronic applications.

1. INTRODUCTION

Nanomaterials are still attracting the attention of people all over the world due to their unique physicochemical properties, which make them suitable for many technological applications.[1] Additionally, nanomaterials introduce the possibility of acquiring new properties, such as optical, electronic, mechanical, magnetic, and chemical reactivity, that are attributed to the reduction of the size of a material to the nanoscale.[2]

Among different nanomaterials, ferroelectric nanotubes are considered to be of great importance because of their use in several applications, including nonvolatile memories, sensors and piezoelectric actuators,[3] and electro-optic and photonic devices. In addition, ferroelectric nanotubes are becoming more interesting for nanosized actuator piezoelectric scanners[4] because they possess remnant polarization[5] and piezoelectric hysteresis.[6−8] However, while lead zirconate titanates (Pb-$(Zr,Ti)O_3$ or PZT) are the most suitable materials for these applications, they are harmful to the environment as lead oxide is deposited during the evaporation process.[9] This makes lead-free ferroelectric materials of even greater interest and, consequently, their development is a big challenge for scientists.[10]

Titanate nanotubes ($Na_2Ti_3O_7$) are promising ferroelectric materials that could be used in place of PZT. $Na_2Ti_3O_7$ is classified as a ferroelectric material, and its structure contains layers of $(Ti_3O_7)^{2-}$, which are associated with Na^+ ions that reside in pseudo-cubic sites, and each layer is joined by the corners and terminal oxygen atoms arranged with only one $\langle TiO_6 \rangle$ octahedron.[11]

Alkali titanates crystallize in a monoclinic structure generalized as $A_2O \times nTiO_2$ $(3 \leq n \leq 8)$, where A is an

Received: May 21, 2022
Accepted: July 8, 2022
Published: July 26, 2022

© 2022 The Authors. Published by American Chemical Society

alkali metal. Nanowires and titanate nanotubes are favorable for many applications, such as gas sensors, photocatalysis, high-energy cells, and environmental purification. The optical and catalytic properties of as-prepared nanotubes can be modified using the metal ion-exchange method. In this method, Na^+ cations in sodium titanate nanotubes are replaced by different metal cations to form the desired metal-doped titanates, which can be used for different modern applications.[12,13]

This work explores the effect of cation exchange in Na-TNTs with different transition metal ions on their dielectric properties, electronic structures, and optoelectronic properties. Nanotube morphology was chosen due to the catalytic activity associated with the tubular shape and the crystalline anisotropy, which motivated us to depict the existence of a net dipole moment along the tube axes.[14] Another reason for choosing these nanostructures is that the distribution of surface charge in either doped or undoped nanotubes leads to increased polarizability through Maxwell−Wagner and interfacial polarization.[15] The ease of preparation in a short duration of time and without the need for high-temperature annealing conditions, as well as the simplicity of raw materials and their low cost, also encouraged us to investigate TNTs. The exchange of Na with different metal ions was carried out for the first time to experimentally investigate physical properties in the frequency range of 50 Hz to 5 MHz and to simulate the same properties from (2.4×10^6−1.8×10^{10} MHz)/(0.1−70 eV) at room temperature. This study is a good opportunity to find out about and examine lead-free ferroelectric materials and simple sustainable solutions for a healthier environment.

2. EXPERIMENTAL STUDY

2.1. Preparation of Titanate Nanotubes. Na-TNTs were prepared using a common hydrothermal method.[16] First, 500 mL of 10 N NaOH was mixed with 10 g of pure anatase-phase titanium dioxide nanoparticles. The NaOH reacted with TiO_2 to produce nanosheets, which were grown in an anisotropic way, presenting faster growth along the *b*-axis. This preferred growth behavior allows the sheets to roll into tubes, transforming 2D into 1D morphology.[11]

The mixture was then exposed for 30 min of magnetic stirring until a white suspension was visualized. The mixture was placed into a Teflon-lined autoclave (1000 mL capacity) and placed in an oven at 160 °C for 23 h. Then, the obtained sample was washed using distilled water. To obtain Na-TNTs, the sample was dried at 100 °C for 12 h.

2.2. Preparation of Metal-Doped Titanate Nanotubes. The as-prepared Na-titanate has the advantage that the sodium ions (Na^+) in the structure are exchangeable; therefore, by mixing with different solutions of metal salts, the Na^+ ions are easily replaced by other metal cations. In this work, to prepare metal-doped nanotubes, the as-prepared Na-TNTs were mixed with metal salts in a w/w ratio of 1:4. Copper sulfate heptahydrate, chromium acetate, nickel acetate, and zinc sulfate heptahydrate were mixed with Na-TNTs to produce Cu-TNTs, Cr-TNTs, Ni-TNTs, and Zn-TNTs, respectively. The simple sonochemical method used here is the main technique implemented for preparing doped samples,[17] where the mixtures were exposed to ultrasonication with a probe sonicator (20 kHz, pulsed mode with 9.9 s on and 3 s off) for 15 min. To remove unreacted sodium salts, the obtained samples were then washed several times with bidistilled water. Finally, the samples were dried at 100 °C for 12 h.

2.3. Electrical Property Measurements. The obtained powders were ground for 30 min using an agate mortar to achieve a very fine powder. Next, the powders were pressed into pellets using a press with a pressure of 1.5×10^6 N/m^2[18] to obtain very compacted discs with diameters of 10.7 and 1.5 mm thickness. The surfaces of each pellet were coated with conducting silver paint on both sides and then checked for good conduction. The two-probe method with a homemade holder was used for measuring all electrical properties along with a Hioki 3532 Japan LCR meter calibrated in the frequency range of 50 Hz−5 MHz at different temperatures (30−500 °C).

2.4. Computational Details. Ab-initio calculations were made with pseudopotential methods using density functional theory (DFT) via material studio with the CASTEP code.[19] The lattice parameters and the band gap of a Na-TNT were obtained using five different generalized gradient approximation (GGA) functionals:[20] the revised Perdew−Burke−Ernzerhof (RPBE),[21,22] the Perdew−Burke−Ernzerhof (PBE),[23] the Perdew−Wang (1991),[24] the Perdew−Burke−Ernzerhof for solids (PBEsol),[25] and the Wu-Cohen (WC).[26] Calculated values were compared with the experimental crystal parameters to determine the method that gives the most realistic results. The electronic structures and the optical properties of the MNa-TNTs were obtained using the PBEsol functional since it provided more sufficient and accurate data compared to experimental results. The exchange and correlation (XC) functional was calculated using a kinetic energy cut-off of 340 eV with ultrasoft pseudopotentials. All calculations were obtained by spin-polarization. The values of maximum force, self-consistent field tolerance, maximum displacement, and maximum stress were 0.03 eV/Å, 1.0×10^{-5} (eV/atom), 0.001 Å, and 0.05 GPa, respectively. For the Brillouin zone integration, a Monkhorst and Pack grid with $2 \times 4 \times 2$ k-points was used. The calculations were optimized using the GGA + *U* method. To obtain more realistic results, the Hubbard parameter was used. This parameter depicts the effect of electron−electron interaction in transition metal ions with the atomic shell 3d. M. Dudarev et al.[27] first discovered this methodology, which improves the results for the electronic properties. For all calculations, the valence electronic states of Na ($3s^1$), O ($2s^2$, $2p^4$), Ti ($3d^2$, $4s^2$), Ni ($3d^8$, $4s^2$), and Zn ($3d^{10}$, $4s^2$) were considered. The U value was chosen to be 6 eV for the Ni atom[28] and 2 eV for the Zn atom. The partial density of states (PDOS) was integrated and viewed by the interpolation method, in which the DOS results were interpolated onto a finer k-point grid of about $200 \times 200 \times 200$. The instrument broadening was 0.05 eV, and the number of points per 1 eV was 100.

3. RESULTS AND DISCUSSION

3.1. X-ray Diffraction Analysis. The crystal structure of $Na_2Ti_3O_7$ shown in Figure 1a is formed by <TiO_6> octahedrons with a zig-zag-like patterned structure. Na^+ ions exist between these layers and occupy two different crystallographic sites linked to the oxygen anions. In the irregular polyhedron, nine oxygen anions are linked with the Na^+ cations, while the Na^+ cations are positioned in oxygen trigonal prisms at the other site.

A layered structure consisting of the < TiO_6> octahedrons permits Na^+ cations to spread and easily exchange with other

https://doi.org/10.1021/acsomega.2c03170
ACS Omega 2022, 7, 27587−27601

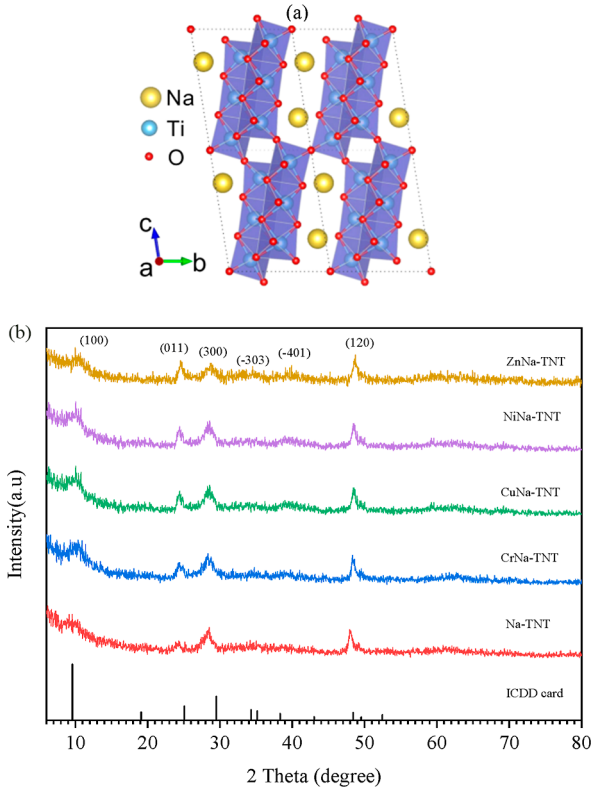

Figure 1. (a) Crystal structure of Na-TNTs and[11] (b) XRD patterns of Na-TNTs, CrNa-TNTs, CuNa-TNTs, NiNa-TNTs, and NaZn-TNTs.

transition element cations (such as Cr, Cu, Ni, and Zn). The ability of this ion exchange is considered a positive feature of $Na_2Ti_nO_{2n+1}$ nanostructures (where $n = 3$).

The XRD patterns of the prepared TNTs are presented in Figure 1b. All the obtained patterns were indexed and compared to ICDD card no. 31−1329. The patterns obtained for all prepared samples prove that TNTs were successfully formed regardless of the doping element. The XRD patterns show the crystalline nature of the TNTs side-by-side with the formation of nanostructure tubular morphology from the strong low-angle reflection at $2\theta = 9.7°$. The peak at 9.7° could be ascribed to the layered structure and/or nanotubes.[11] Accordingly, we concluded that the tubular shape is the predominant contributor when correlating between structures and morphological features. The strong-intensity reflection belonging to the (100) plane is approximately 9.7 Å due to the interlayer distance of sodium titanate. The (100) plane is present for all samples, regardless of their doping type. The existence of the (100) plane confirms that the nanotubular morphology of the obtained samples did not collapse after doping with the transition metals (Cr, Cu, Ni, Zn).

The intensity of the (100) plane is affected by the dopant type and confirms that the M cations (Cr^{2+}, Cu^{2+}, Ni^{2+}, and Zn^{2+}) were successfully exchanged with Na^+ ions. The change in the intensity of the (011) plane emphasizes the exchange process, in addition to the splitting of the (300) plane for all samples. The lattice parameters were calculated using the unit cell software program and according to monoclinic symmetry, as shown in Table 1. The result confirms that the Na^+ ions were successfully exchanged with different cations (Cr^{2+}, Cu^{2+}, Ni^{2+}, and Zn^{2+}), resulting in an increase in unit cell volume.

Table 1. Calculated Lattice Parameters, Angle β, and Unit Cell Volume (V) of TNT Materials

TNT	lattice parameters				
	a (Å)	b (Å)	c (Å)	°β	V (Å)^3
Na-TNT	9.00	3.76	11.21	101.48	372.81
CrNa-TNT	9.23	3.78	12.42	91.89	433.62
CuNa-TNT	9.38	3.79	11.08	101.99	386.00
NiNa-TNT	9.29	3.72	13.09	88.85	452.93
ZnNa-TNT	9.41	3.75	12.63	90.61	446.75

According to Shannon,[29] the ionic radii of Na^{1+}, Ti^{4+}, Cr^{2+}, Cu^{2+}, Ni^{2+}, and Zn^{2+} are 0.99, 0.42, 0.80, 0.57, 0.55, and 0.60 Å, respectively. Thus, the transition metal cations were probably substituted on the Ti^{4+} site since they all have ionic radii larger than Ti^{4+} and smaller than Na^{1+}. Although the Cr^{2+} cation has the largest ionic radius, it has a smaller unit cell volume than the Ni^{2+}- and Zn^{2+}-doped samples, which may be because it substituted some of the Na^{1+} and Ti^{4+}.

3.2. Morphological Structure. *3.2.1. Field-Emission Scanning Electron Microscopy (FESEM).* Figure 2a−e display FESEM−EDS results corresponding to Na-TNTs, CrNa-TNTs, CuNa-TNTs, NiNa-TNTs, and NaZn-TNTs, respectively. In all FESEM images, the nanotubes have identical diameters but differ in length. The nanotubes appear to be randomly assembled with no orientation or connection with each other. As obtained from FESEM images, the NiNa-TNT and NaZn-TNT powders were more agglomerated than the other powders. The EDXS spectra confirm the exchange process and indicate that a portion of Na cations still exists in the samples. These obtained data reveal that the tubular form of the prepared samples did not change, despite the occurrence of the exchange process. The data reveal that most Na cations were replaced partially with the other cations due to the observed uniform distribution of Cr^{2+}, Cu^{2+}, Ni^{2+}, and Zn^{2+}. Small peaks of Na can be observed in all samples and indicate incomplete exchange.

3.2.2. High-Resolution Transmission Electron Microscopy (HRTEM). Figure 2f,g represents HRTEM images for Na-TNT and NiNa-TNT, respectively. All HRTEM images indicate a nanotube morphological structure that is multiwalled and open-ended.

3.3. Thermal Properties. *3.3.1. Thermal Gravimetric Analysis.* Thermal gravimetric analysis (TGA) is a common technique for obtaining the thermal stability of a material. TGA thermograms of the TNTs are presented in Figure 3, wherein the temperature ranges from room temperature to 500 °C. The pure and doped TNTs exhibit three-step decomposition discussed after adding a derivative curve (dTG). The first weight loss step was observed at about 117.9 , 168.2 , 115 , 112, and 128 °C with the corresponding weight losses of 5.5, 7.3, 4.14, 3.8, and 4.9% for Na-TNTs, CrNa-TNTs, CuNa-TNTs, NiNa-TNTs, and ZnNa-TNTs, respectively. This step is attributed to the loss of absorbed moisture.[30] The second weight loss step in the same material order was observed at 216.6, 358, 212, 207, and 250 °C with weight losses of 2.96, 2.4, 4.3, 2.5, and 3.6%, respectively. This step is attributed to the dehydration of interlayer water.[31] The final step was above 300 °C for the Na-TNTs and ZnNa-TNTs, above 200 °C for the CuNa-TNTs and NiNa-TNTs, and above 400 °C for the CrNa-TNTs. This step corresponded to an insignificant weight gain of ∼0.9 and 0.4%) for the Na-TNTs and NiNa-TNTs,

https://doi.org/10.1021/acsomega.2c03170
ACS Omega 2022, 7, 27587−27601

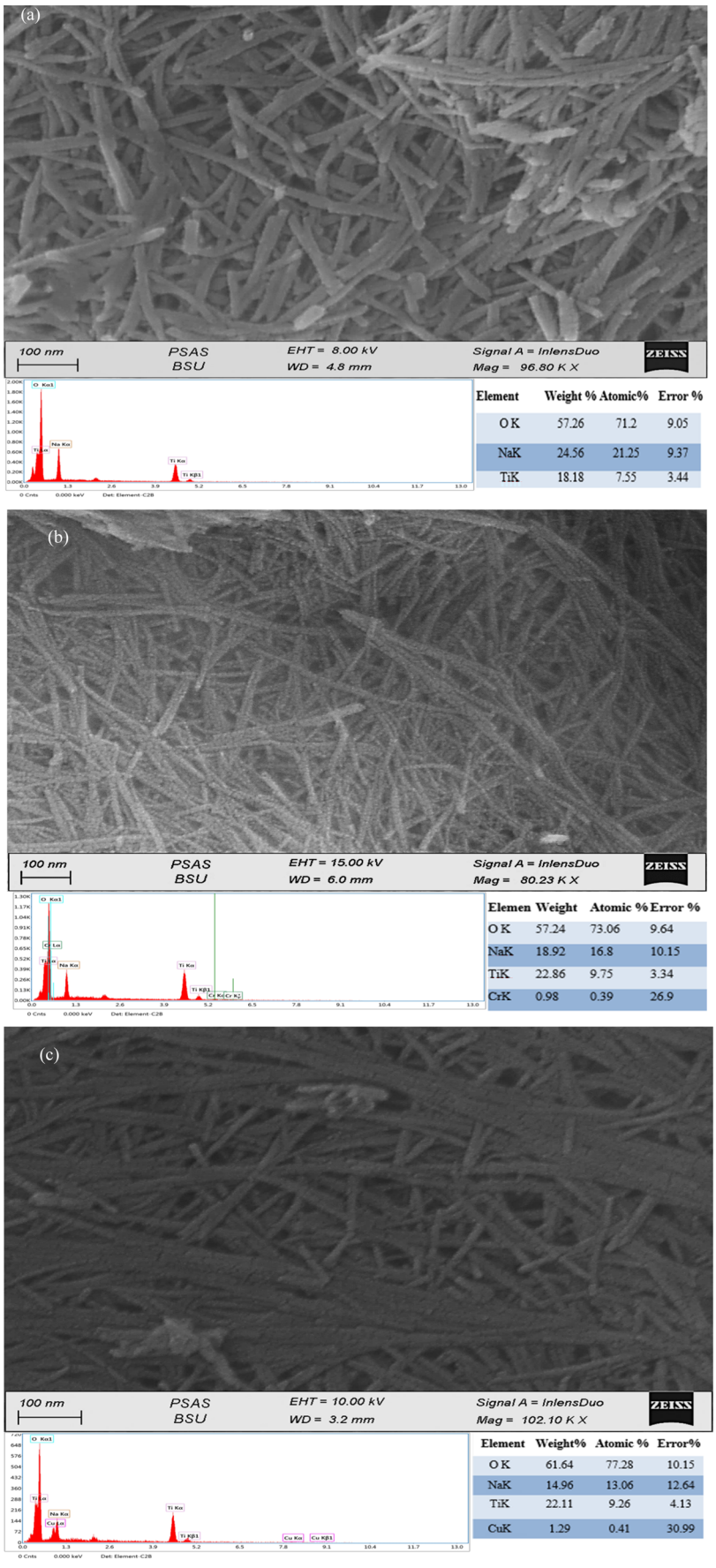

Figure 2. continued

https://doi.org/10.1021/acsomega.2c03170
ACS Omega 2022, 7, 27587−27601

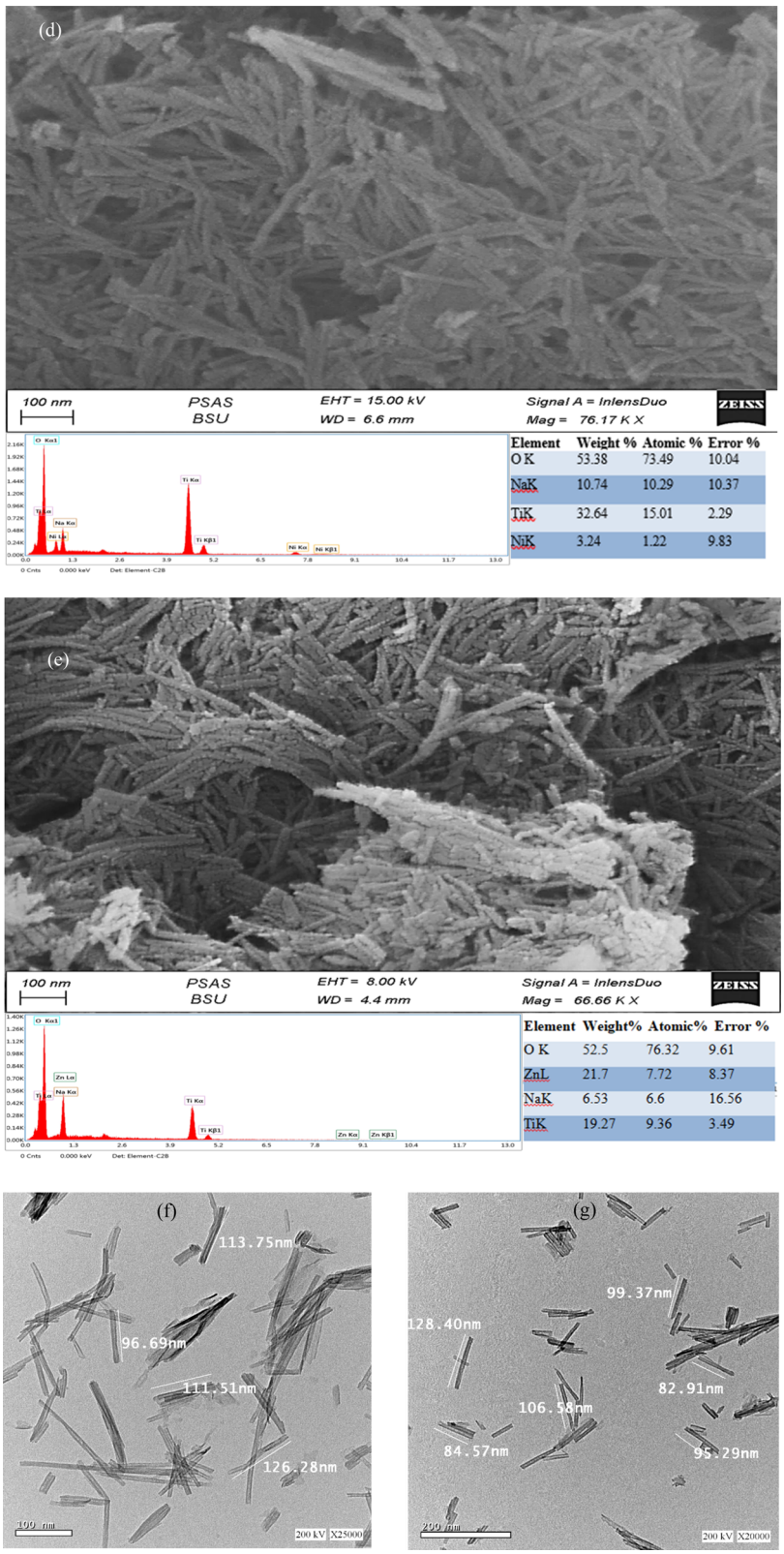

Figure 2. FESEM−EDS images for Na-TNTs (a), CrNa-TNTs (b), CuNa-TNTs (c), NiNa-TNTs (d), and NaZn-TNTs (e) and HRTEM for Na-TNTs (f) and NiNa-TNTs (g).

respectively, and a weight loss of ∼0.4% for the CrNa-TNTs, CuNa-TNTs, and ZnNa-TNTs.

3.4. Dielectric Properties. Figure 4a−e represent thermal variation of the real part of the dielectric constant (ε') for the prepared samples at two selected frequencies (400 kHz and 2 MHz), and Figure 5f shows the room-temperature frequency dependence of ε'. The results could be divided into four main regions. The first region is the increase of ε' versus temperature until the peak value is reached, which was observed to depend on the type of doped transition metals. The number

https://doi.org/10.1021/acsomega.2c03170
ACS Omega 2022, 7, 27587−27601

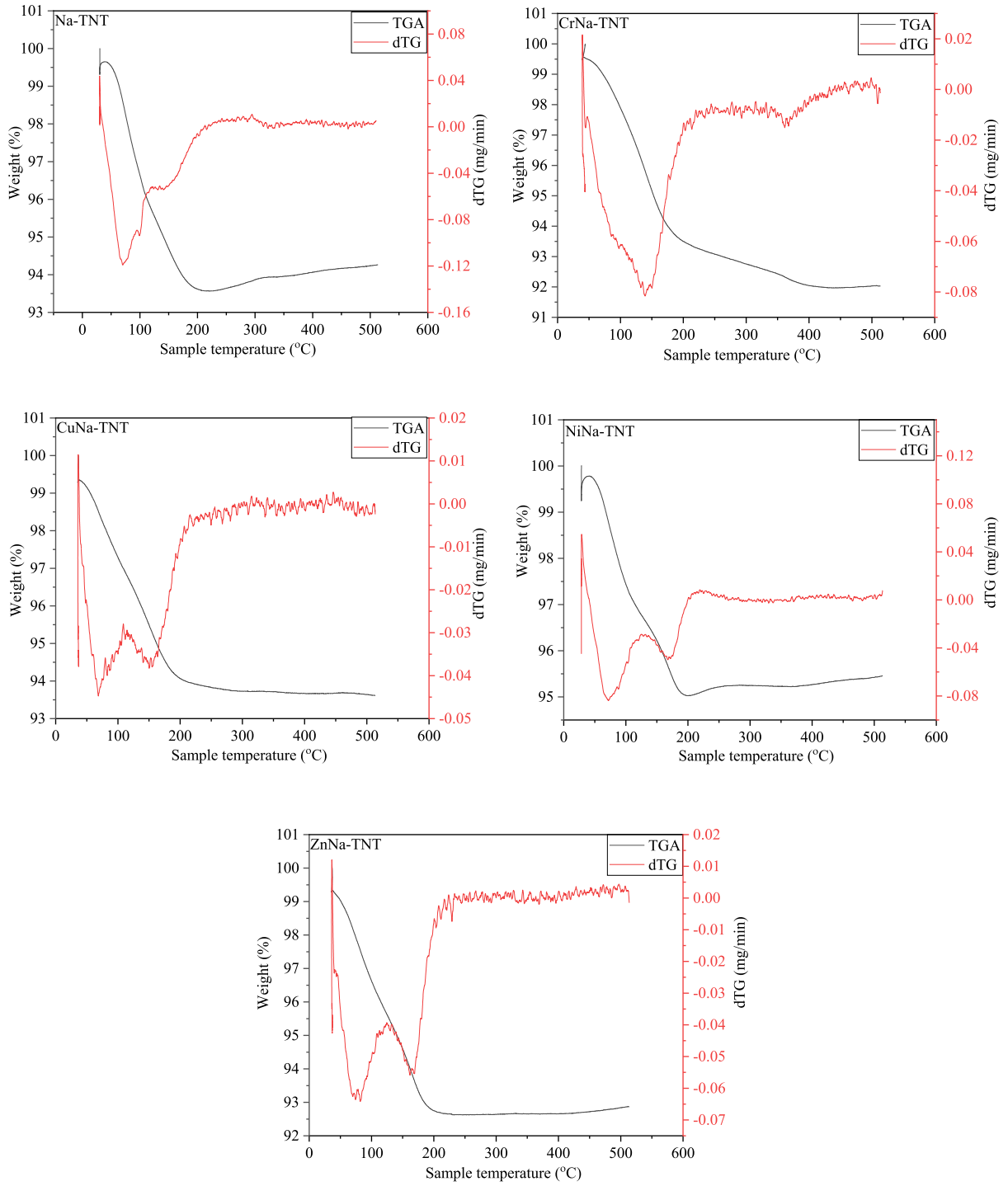

Figure 3. TGA-dTG curves for Na-TNTs, CrNa-TNTs, CuNa-TNTs, NiNa-TNTs, and NaZn-TNTs.

corresponding to this peak position and its width could be ascribed to different transitions occurring in the nanotubes, either doped or undoped. The first peak is located between values of 50 and 95 and is attributed to the dehydration of adsorbed water. The second peak is located between 150 and 300 and is attributed to the first phase transition since the TNTs are transformed into TiO_2.[32] The third peak is above 350 and is attributed to the deformation of the nanotube and the loss of the tubular shape.[33] The dipoles are unable to orientate with the field at low temperatures, resulting in a prosaic polarization and a decrease in ε'. When the temperature starts to increase, a number of bound dipoles are released, which then participate in the process of polarization. The mobility of these dipoles then increases, which results in the increase of the ε' value.[34] As obtained from Figure 4a−e, the Na-TNTs and Zn-TNTs have more than one transition. Unlike the Cr-TNTs, Cu-TNTs, and Ni-TNTs, the phase transition is clearer at approximately 450 °C for the Cr-TNTs and Ni-TNTs and at 250 °C for the Cu-TNTs.

Figure 5 displays the temperature dependence of the loss tangent (tan δ) for the prepared nanotubes at the two selected frequencies (400 kHz and 2 MHz). Tan δ is attributed to the

https://doi.org/10.1021/acsomega.2c03170
ACS Omega 2022, 7, 27587−27601

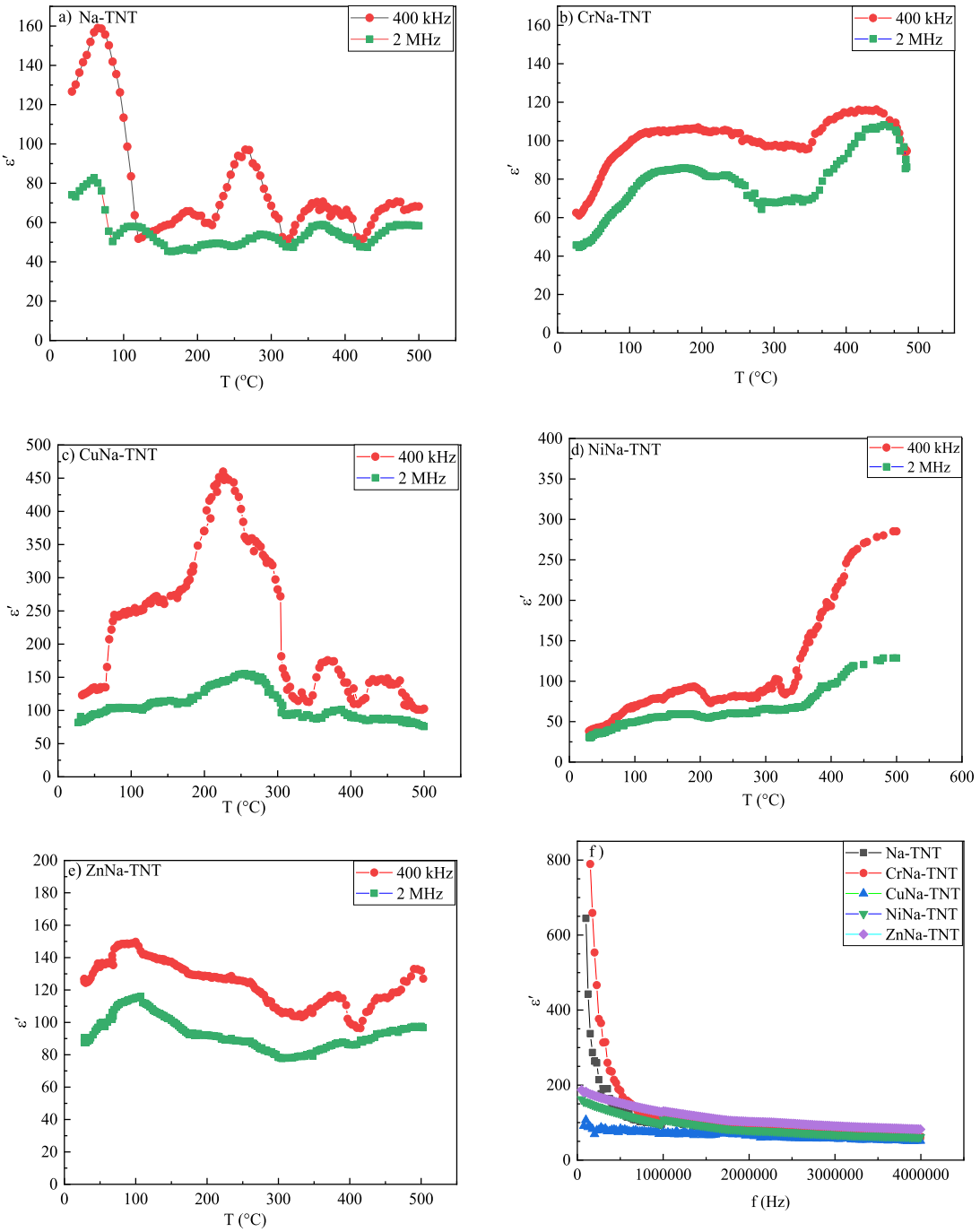

Figure 4. (a–e) Real part of the dielectric constant ε' for sodium titanate nanotubes and their doped derivatives and, (4f) the room-temperature frequency dependence of (ε').

energy loss in a dielectric material when polarization remains after an applied field. For the Na-TNTs, CuM-TNTs, and NiM-TNTs, tan δ is high at low frequencies and low at high frequencies. This is attributed to the fact that the number of polarized dipoles is inversely proportional to the frequency. At a high frequency, the small polarization value is attributed to rare polarization processes. Regarding the tan δ temperature dependence, the nanotubes have two types of losses.[35] Conduction loss is indicated by a soft curve, and at a certain temperature of relaxation loss, a peak is obtained. The conduction loss is related to random dipole interactions with each other. Meanwhile, the relaxation loss is a competition between two temperature influences: (1) friction decrease due to the lack of material viscosity (loss decreases)[36] and (2) the increase in dipole friction (loss increases). For all samples, tan δ exhibits many maxima and minima within the temperature range.

Figure 6 displays the temperature dependence of the ac conductivity, σ_{ac}, for the prepared nanotubes at the two selected frequencies (400 kHz and 2 MHz). The σ_{ac} values of the MNa-TNTs were computed from resistance values, $\varrho = (R^*A)/d$, where R is the resistance, A is the area, d is the thickness, and σ is the conductivity, which is $\sigma = 1/\varrho$.[37] Above 300 °C, the electrical conductivity behavior corresponds to TiO_2.[32] In general, the calculated σ_{ac} for all MNa-TNTs exhibits many maxima and minima within the temperature

https://doi.org/10.1021/acsomega.2c03170
ACS Omega 2022, 7, 27587−27601

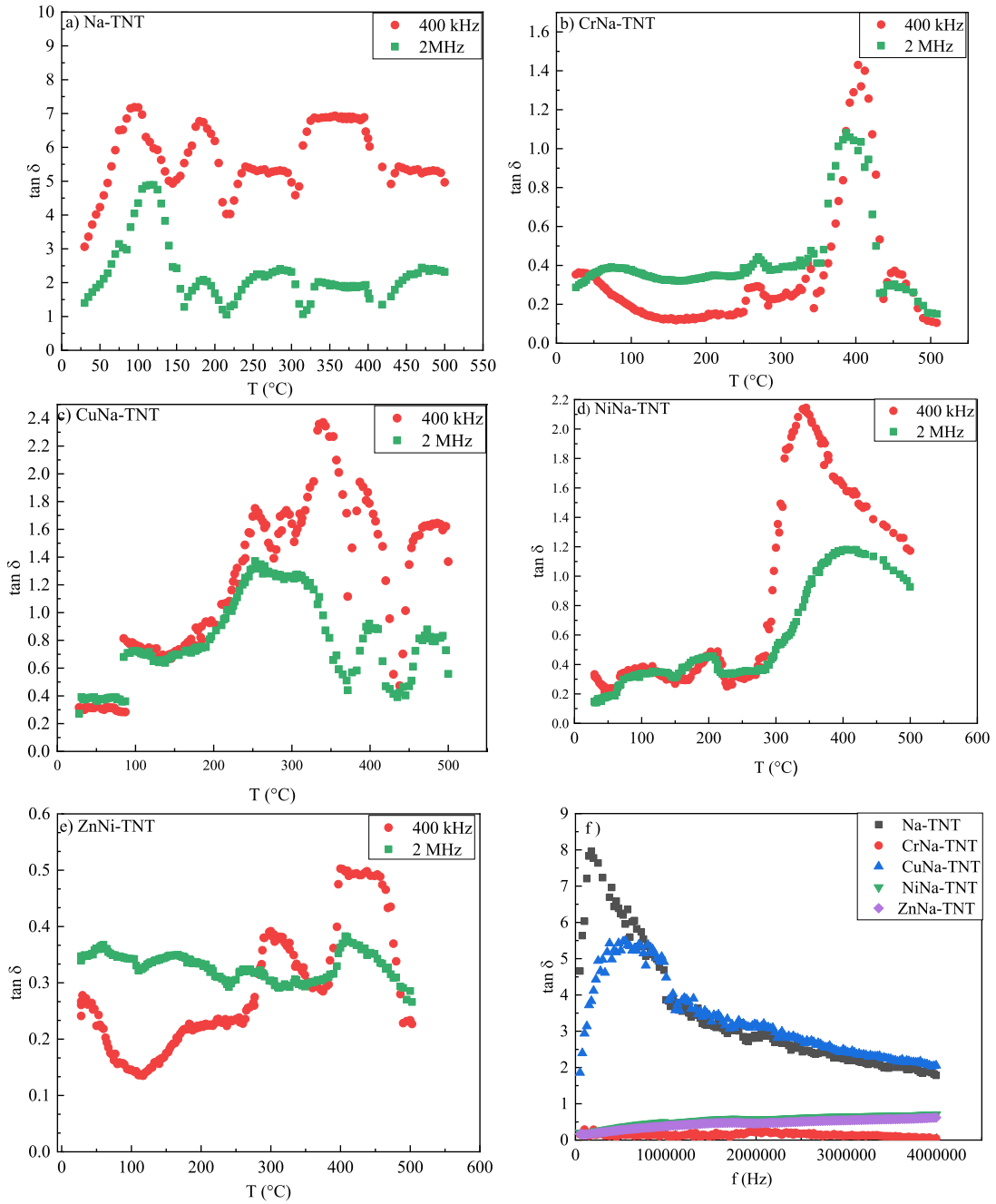

Figure 5. (a−e) Dependence of the dielectric loss tangent tan δ for sodium titanate nanotubes and their doped derivatives and (5f) the room-temperature frequency dependence of tan δ

range. The maximum conductivity for Na-TNTs, CrNa-TNTs, CuNa-TNTs, NiNa-TNTs, and ZnNa-TNTs was 0.045, 0.115, 0.020, 0.012, and 0.004 Ω^{-1} m^{-1} at 130, 420, 250, 400, and 120 °C, respectively. This behavior is due to generation of different types of dipoles.[38] For example, in the case of the CuNa-TNTs, the first type of dipole is expected to be generated due to the substitution of Cu^{2+} and Cu^{1+} at Ti^{4+} sites. The second type of dipole resulted from the interlayer spacing of both the doped derivatives.[39]

Figure 7 represents lnσ as a function of 1000/T for the MNa-TNTs. The data revealed two different straight lines with different slopes pointing to the existence of two conduction mechanisms[13,40] at the low- and high-temperature regions. At a low temperature, the conduction appears to be characteristic of the host and is associated with the hopping process, including the free electrons from $Ti_3O_7^{2-}$ groups that jump from one Ti−Ti chain to another adjacent one. Such a process would involve low activation energy; therefore, a small slope value is observed in this region. The small slope for the Cr-TNTs and Zn-TNTs in the low-temperature region reveals the formation of a configuration that diminishes the number of loose electrons, appreciably reducing electronic hopping conduction. The ionic conductivity of the exchangeable interlayer appears to be prominent in this region for the Cr-TNTs. However, for the Na-TNT, Cu-TNT, and Ni-TNT samples, the ionic conduction of this interlayer is less pronounced.

The continuous growth observed in the conductivity can be explained by assuming that the cations, which are exchanged at

https://doi.org/10.1021/acsomega.2c03170
ACS Omega 2022, 7, 27587−27601

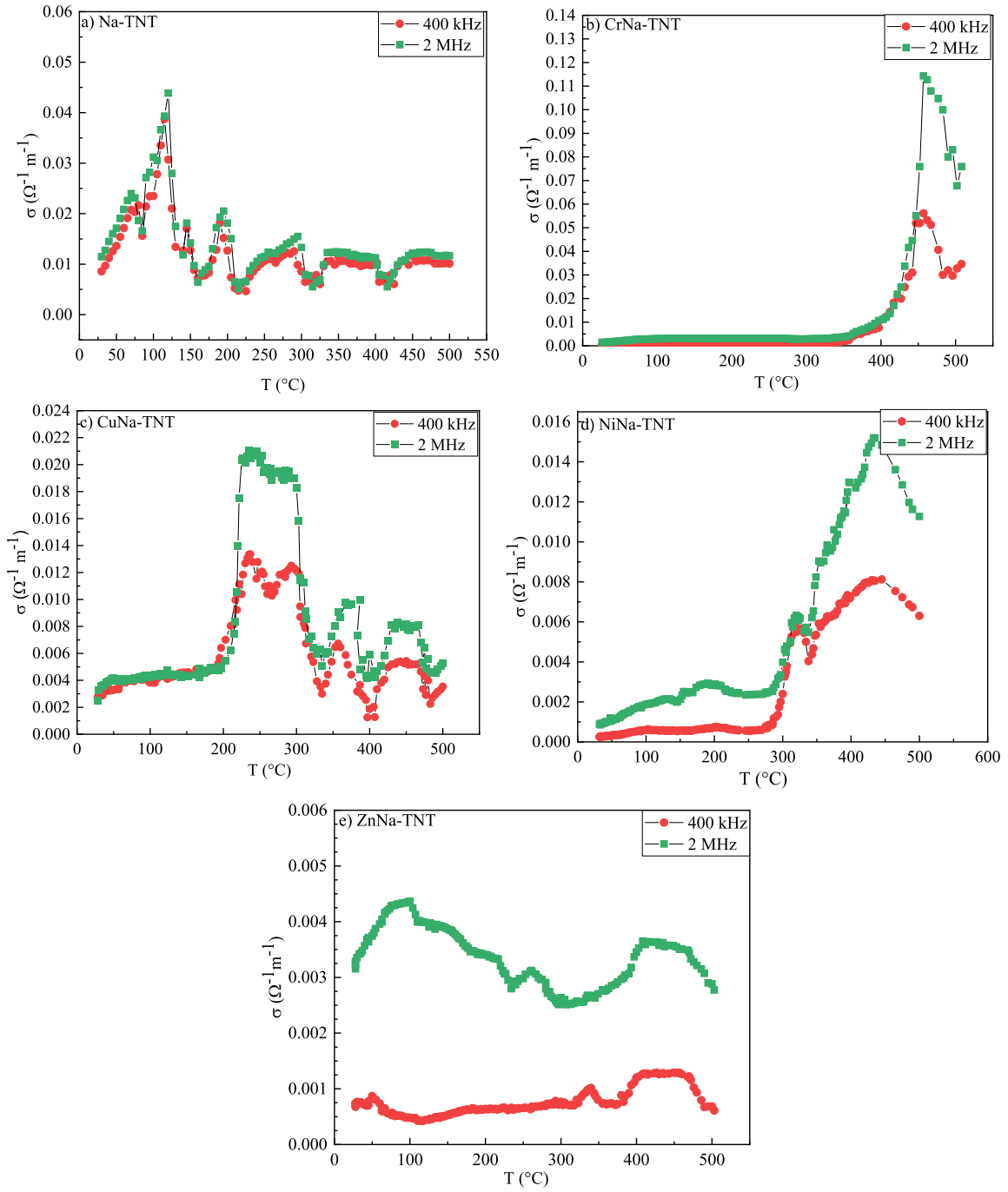

Figure 6. (a–e), Dependence of AC conductivity (σ) for sodium titanate nanotubes and their doped ones as a function of temperature (°C).

Ti^{4+} sites, are in the valence state (Cu^{2+}), and their exchange would naturally cause the number of free electrons to noticeably increase and to jump from Ti–Ti chains via conduction. Thus, the conduction via electronic hopping in this region may be exogenous or dopant dependent. In the high-temperature region, the higher slope is related to ionic conduction[40] since the oxygen from $Ti_3O_7^{2-}$ groups participates in the conduction mechanism in this region.[39]

Table 2, represents the measured activation energies of the NaM-TNTs, while those values calculated from the experimental data are provided in Table 1. The small activation energy values in the low-temperature region (~150) are attributed to the electronic conductivity. The increment in the activation energy in the second region (~350 °C) indicates ionic conductivity. The Cu-doped sample shows high values of activation energy among all prepared samples. Cu^{1+} and Cu^{2+} valence exchange occurs in this sample, and hopping between the cations is very probable. The lowest value of activation energy in the low-temperature region corresponds to Zn-doped Na-TNTs as they did not reveal any valence variations. Zn ions do not belong to the transition element series. One could expect that ionic conduction dominates at relatively high temperatures. Thus, these materials are applicable for use in fuel cell applications.[41]

Finally, doping with these transition metals leads to different electronic properties due to the different dopant ionic radii and different occupancy preferences, in addition to the variation of the lattice constant, bond length, and bond angle. On the other

https://doi.org/10.1021/acsomega.2c03170
ACS Omega 2022, 7, 27587–27601

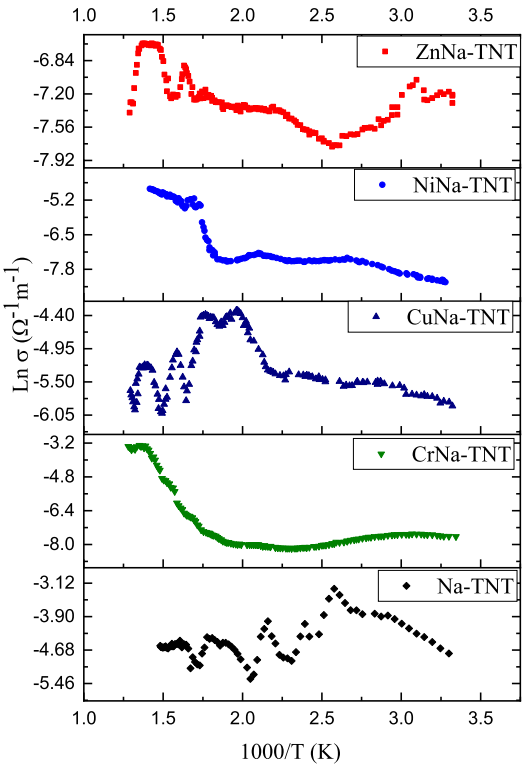

Figure 7. Dependence of Ln ac conductivity (Ln σ) for MNa- TNT nanotubes on the reciprocal of absolute temperature at 400 kHz.

Table 2. Calculated Values of Activation Energies (E_1) and (E_2) at Low (0−150°C)- and High (150−350 °C)-Temperature Regions, Respectively, of NaM-TNT Materials at 400 KHz

TNT materials	activation energy	
	E_1 (eV)	E_2 (eV)
Na-TNT	0.17	0.41
CrNa-TNT	0.04	0.86
CuNa-TNT	0.43	0.49
NiNa-TNT	0.12	0.15
ZnNa-TNT	0.03	0.52

hand, the splitting of the (100) and (011) planes in all samples, as shown in Figure 1b, could be the main reason for such variation in the electronic results.

3.5. Computational Study. Table 3, reports the calculated lattice constants for the Na-TNTs that were obtained using the investigated XC functionals and the experimental crystal parameters. From Table 3, the PBEsol functional exhibits better agreement with the experimental results when the pseudopotential is treated with the ultrasoft method. Thus, to analyze and discuss the electronic and optical properties, the PBEsol functional was used. Figure 8 represents the optimized structures (GGA/PBEsol) of $MNaTi_3O_7$ ($Na_4Ti_6O_{14}$, $NiNa_2Ti_6O_{14}$, and $ZnNa_2Ti_6O_{14}$).

By using the semiempirical dispersion correction D2 (DFT/PBE-D2), Galvan et al.[28] reported that the band gap value of a NiNa-TNT was 2.8 eV and was close to the experimental value (2.86 eV). The band gaps (E_g) of the Na-TNTs, NiNa-TNTs, and ZnNa-TNTs were calculated using PBEsol with ultrasoft pseudopotentials; the values were 3.2, 2.4, and 3.3 eV, respectively, as shown in Figure 9. The low band gap value of NiNa-TNTs can be seen in their yellowish beige color, suggesting that this material may be useful for applications in solar cells and photocatalysis.[42]

Figure 10 illustrates the PDOS of NaM-TNTs that were calculated using the DFT + U method. Near the Fermi level of the NiM-TNT, high-electronic state hybridization between the Ti (3d), O (2p), and Ni (3d) states was observed and was responsible for the narrowing of the NiNa-TNT band gap value. Large contributions of Ni (3d) electronic states exist below the Fermi level (valence band). Finally, the O (2p) and Ti (3d) states of the ZnNa-TNT exist at the edge of the valence band, and the Zn (3d) doping contribution was below the conduction band. For all compounds, the high contribution to the valence states is related to the O (2p) states, while the conduction states are dominated by Ti (3d) atoms. Therefore, the conduction is mainly due to the transition from O (2p) states to Ti (3d).

The optical properties of MNa-TNTs were calculated theoretically at photon energies ranging from 0.01 to 70 eV, while those of the experimental studies were calculated at values lower than 0.01 eV. Figure 11 introduces the reflectivity spectra of the MNa-TNTs as a function of photon energy from 0.01 to 50 eV. At 0.01 eV (infrared region), the obtained reflectivity of the Na-TNTs, NiNa-TNTs, and ZnNa-TNTs was ∼0.145. The reflectivity then increases dramatically to ∼0.28 as photon energy increases. The reflectivity of the MNa-TNTs has maximum values in the range of 6.5 to 12 eV, and the Na-TNTs have the highest value (∼9.9 eV). The reflectivity reached almost zero beyond 45 eV. In the range of 12−45 eV, small peaks with a maximum of ∼0.199 at 22.6 eV were observed for NiNa-TNTs.

Absorption spectra are useful for solar energy applications to achieve optimum efficiency. Figure 12, introduces the absorption spectra of the MNa-TNTs. The nanotubes reveal good absorption coefficients from 2.5 to 25 eV. The Na-TNTs, ZnNa-TNTs, and NiNa-TNTs have a maximum value of 8.2 eV. Among these materials, the ZnNa-TNTs have the lowest absorption coefficient value. The Na-TNTs possess two maximum values of 8.2 and 36.6 eV. The MNa-TNTs showed strong absorption in the range of 34−40 eV (UV region) with

Table 3. Comparison Between the Calculated and Experimental Lattice Constants of $Na_2Ti_3O_7$

functionals	Ultrasoft					norm-conserving				
	a (Å)	b (Å)	c (Å)	v (Å^3)	band gap (eV)	a (Å)	b (Å)	c (Å)	v (Å^3)	band gap (eV)
PBE	8.426	3.789	9.091	283.37	3.169	8.387	3.769	9.036	278.76	3.351
RPBE	8.804	3.837	9.358	309.65	2.996	8.757	3.815	9.294	304.10	3.158
PW91	8.545	3.790	9.146	290.00	3.128	8.515	3.767	9.074	284.90	3.340
WC	8.619	3.792	9.137	292.39	3.155	8.598	3.771	9.081	288.21	3.330
PBEsol	8.607	3.786	9.132	291.39	3.172	8.578	3.768	9.076	287.18	3.338
EXP[44]	8.571	3.804	9.135	291.78	3.3					

https://doi.org/10.1021/acsomega.2c03170
ACS Omega 2022, 7, 27587−27601

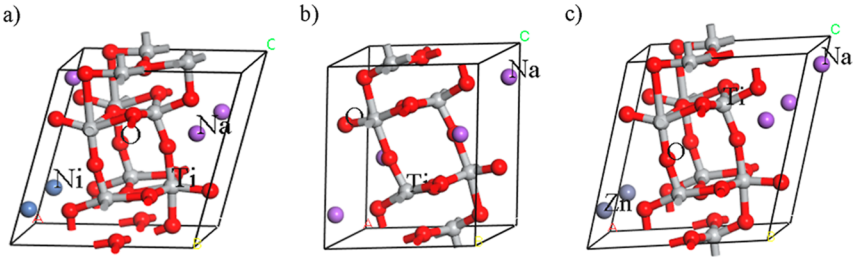

Figure 8. Optimized crystal structures of MNa-TNT compounds using the GGA/PBEsol method; (a) NiNa-TNT, (b) Na-TNT, and (c) ZnNa-TNT.

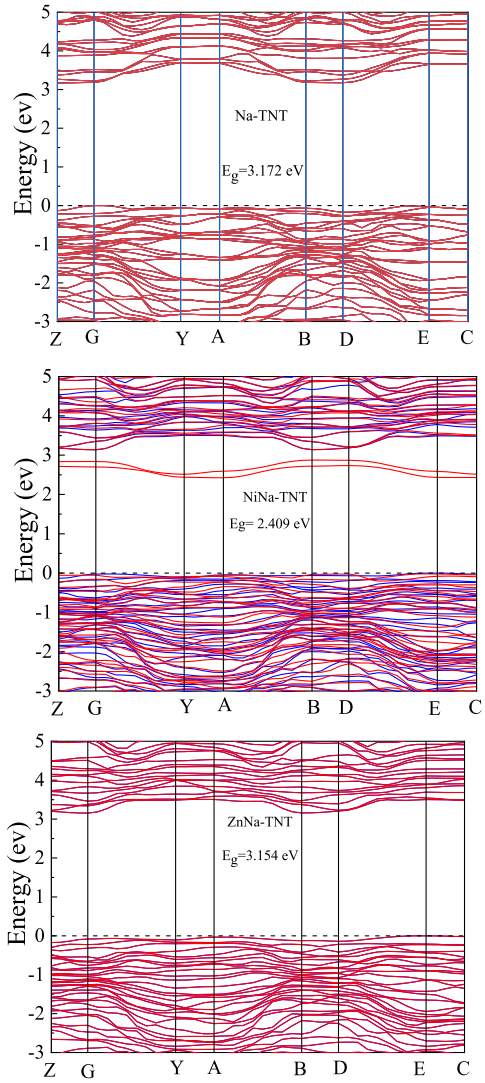

Figure 9. Band structures of the MNa-TNT compounds using GGA/PBEsol/ultrasoft, where the blue and red colors refer to alpha and beta states, respectively.

a maximum absorption of 37 eV. Therefore, these materials will be photoactive in the UV region.[43]

Figure 13a,b shows the real part of the refractive index and extinction coefficient (imaginary part) for the MNa-TNTs. The MNa-TNTs display high values of $n(\omega)$ and $k(\omega)$ at photon energies of 3.8 and 8.08 eV, respectively, which decrease in the UV region. The n (ω) values of the Na-TNTs, NiNa-TNTs, and ZnNa-TNTs were 2.25 at a photon energy of ~0.01 eV.

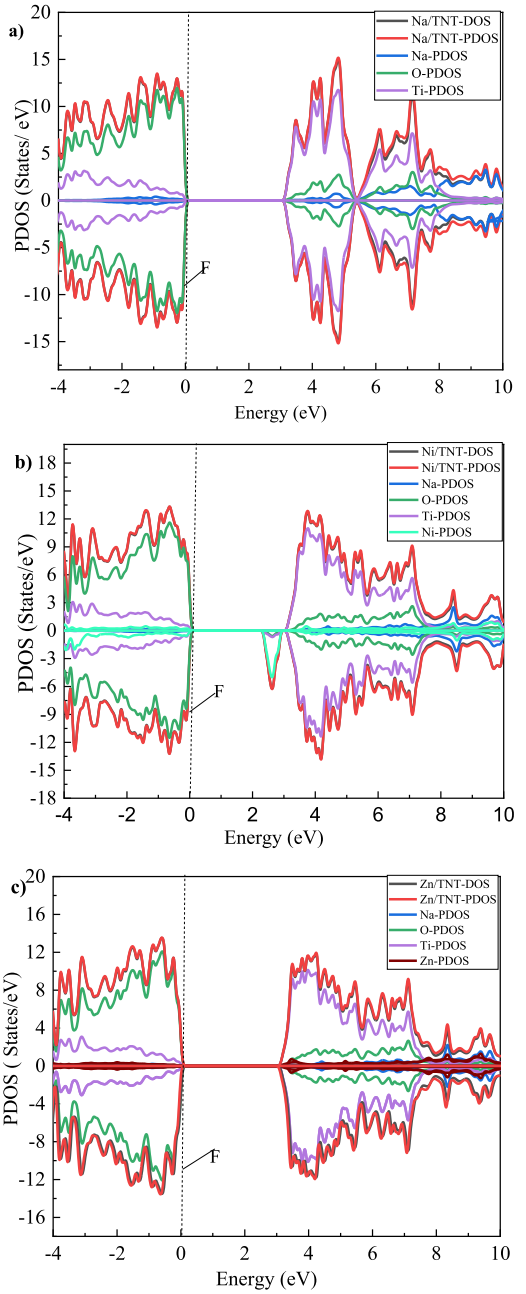

Figure 10. PDOS of the MNa-TNT materials using GGA/PBEsol/ultrasoft, and the dashed line is the Fermi level; (a) Na-TNT, (b) NiNa-TNT, and (c) ZnNa-TNT.

Figure 14 shows the obtained dielectric functions, ε_1 (ω) and ε_2 (ω), for the nanotubes. For Na-TNTs, ε_1 (ω) was

https://doi.org/10.1021/acsomega.2c03170
ACS Omega 2022, 7, 27587−27601

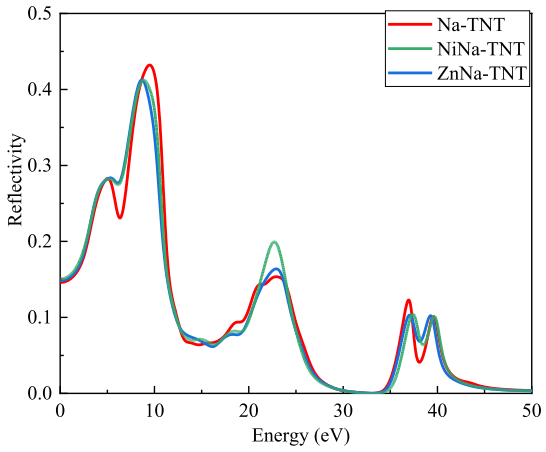

Figure 11. Calculated reflectivity of MNa-TNT materials as a function of energy (eV) using GGA/PBEsol/ultrasoft.

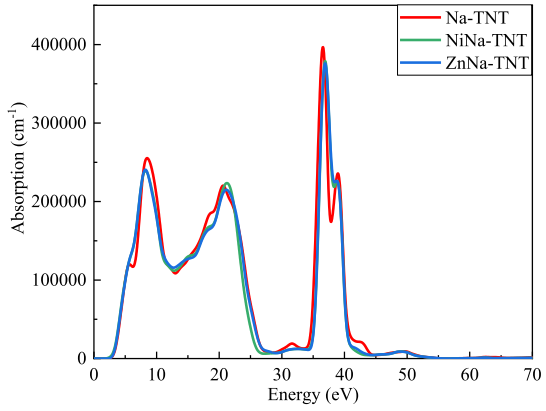

Figure 12. Absorption (cm^{-1}) of MNa-TNT compounds as a function of energy (eV) using GGA/PBEsol/ultrasoft.

positive up to 7.8 and 7.4 eV for the ZnNa-TNTs and NiNa-TNTs, respectively. $\varepsilon_1(\omega)$ reveals a characteristic peak at 3.8 eV for the Na-TNTs, ZnNa-TNTs, and NiNa-TNTs and at 6.8 eV for the Na-TNTs. The compounds display dielectric and metallic behavior when $\varepsilon_1(\omega) > 0$ and $\varepsilon_1(\omega) < 0$, respectively. At a photon energy of 0.05 eV, the dielectric constant values were 5, 5.1, and 5.07 for the Na-TNTs, NiNa-TNTs, and ZnNa-TNTs, respectively.

The imaginary part of the dielectric function is a considerable parameter; it introduces several interstitial−band transitions between the valance band and the conduction band (CBd). Figure 14b shows the imaginary part $\varepsilon_2(\omega)$. A major peak occurs at ∼5.15 and 7.5 eV for the ZnNa- and NiNa-TNTs and the Na-TNTs, respectively.

Figure 15 illustrates the predicted optical conductivity spectra of the MNa-TNTs as a function of photon energy. The obtained optical conductivity reveals high values at high frequencies (UV region). The optical conductivity for all MNa-TNTs displays several maxima and minima within the photon energy range. However, the Na-TNTs exhibit optical conductivity peaks higher than the others.

The energy loss function (L) indicates the energy loss of electrons passing through a material. L covers the entire photon energy range, including scattered photons. In Figure 16 the maximum observed peaks are at 24, 23.5, and 23.6 eV for the Na-TNTs, NiNa-TNTs, and ZnNa-TNTs, respectively. The NiNa-TNTs exhibit the highest peak compared to other nanotubes, while Na-TNTs show the lowest peak, except at 37 eV where they exhibit the highest peak.

4. CONCLUSIONS

Na-TNTs and their metal-doped counterparts were successfully prepared using a simple hydrothermal method. The crystal structure of these nanotubes was classified as monoclinic. The Cu- and Ni-doped samples had larger dielectric values compared with the undoped sample. The dielectric loss of the doped samples was smaller than that of the undoped Na-TNTs, and the lowest value corresponded to the CrNa-TNTs. At 400 °C, the highest conductivity corresponded to the CrNa-TNTs. These nanotubes possess mixed ionic and electronic conductivities, which make them suitable for fuel cell applications. At low temperatures, the CuNa-TNTs possess the highest activation energy. Theoretically, the crystal structure and the optoelectronic properties of the MNa-TNTs (M = Ni and Zn) were obtained using the GGA PBEsol/pseudopotential functional ultrasoft. The values of the band gap for Na-TNTs and NiNa-TNTs were close to the experimental values. The lowest band gap value corresponded to the NiNa-TNTs. Finally, we noticed that there is a significant change in optical properties between these materials; thus, they are favorable for solar cell applications and optoelectronic devices in the UV region.

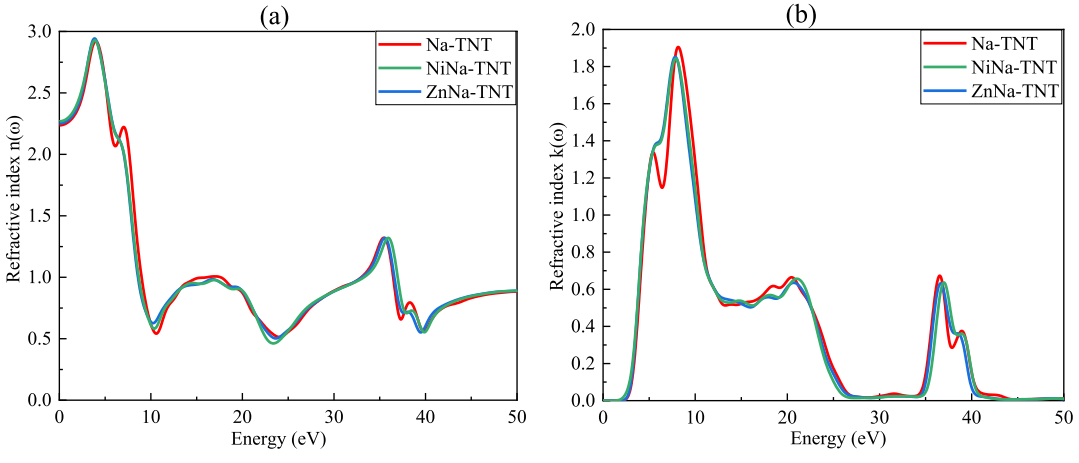

Figure 13. Refractive index (a) and extinction coefficient (b) of MNa-TNT compounds as a function of energy (eV) using GGA/PBEsol/ultrasoft.

https://doi.org/10.1021/acsomega.2c03170
ACS Omega 2022, 7, 27587−27601

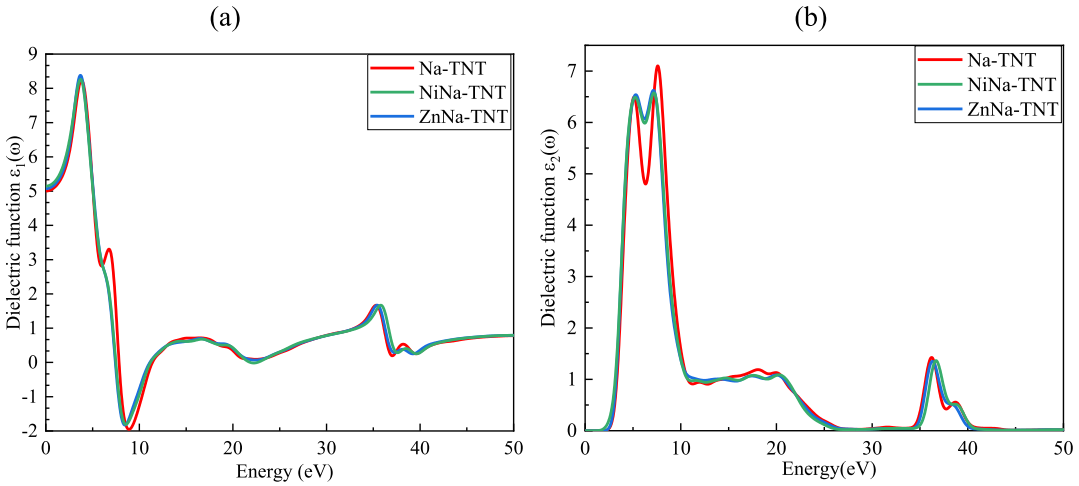

Figure 14. Calculated spectra for (a) real (ε_1 (ω)) and (b) imaginary (ε_2 (ω)) parts of the dielectric function for the MNa-TNT compounds, respectively, using GGA/PBEsol/ultrasoft.

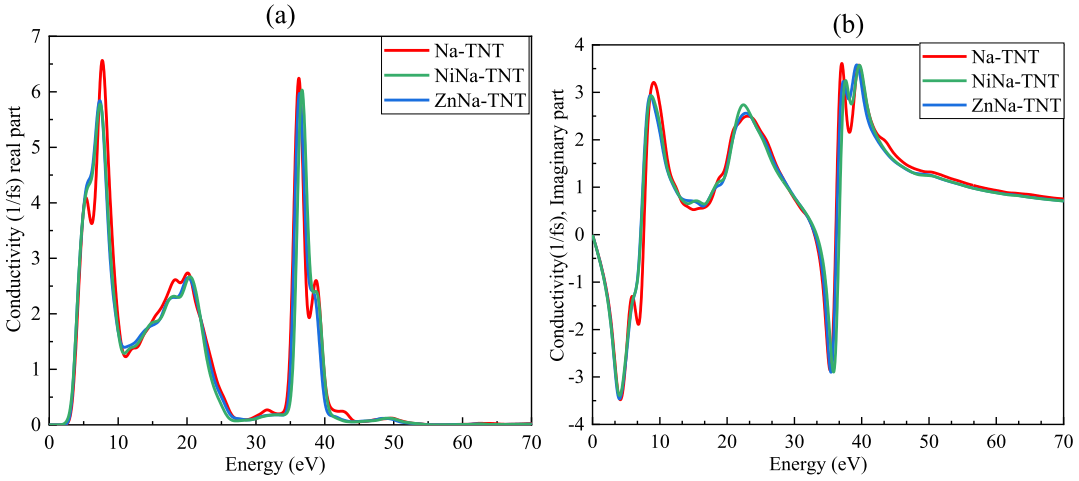

Figure 15. (a) Real part and (b) imaginary part of the optical conductivity spectra for MNa-TNT materials as a function of photon energy using GGA/PBEsol/ultrasoft.

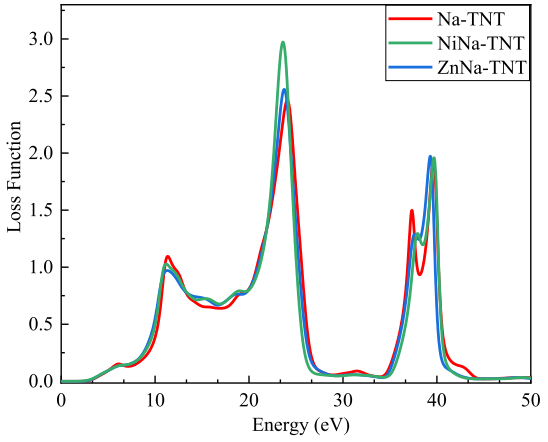

Figure 16. Energy loss function for all MNa-TNT compounds versus photon energy (eV) using GGA/PBEsol/ultrasoft.

AUTHOR INFORMATION

Corresponding Author

Ayman H. Zaki − *Materials Science and Nanotechnology Department, Faculty of Postgraduate Studies for Advanced Sciences, Beni-Suef University, Beni-Suef 2722165, Egypt;* orcid.org/0000-0003-0026-1721; Phone: 002-01225047780; Email: ayman.zaki@psas.bsu.edu.eg, Ayman_h_zaki@yahoo.com

Authors

Hager Samir − *Materials Science and Nanotechnology Department, Faculty of Postgraduate Studies for Advanced Sciences, Beni-Suef University, Beni-Suef 2722165, Egypt*

Mohamed Taha − *Materials Science and Nanotechnology Department, Faculty of Postgraduate Studies for Advanced Sciences, Beni-Suef University, Beni-Suef 2722165, Egypt;* orcid.org/0000-0002-5367-2009

S.I. El-Dek − *Materials Science and Nanotechnology Department, Faculty of Postgraduate Studies for Advanced Sciences, Beni-Suef University, Beni-Suef 2722165, Egypt;* orcid.org/0000-0003-4564-9455

Complete contact information is available at: https://pubs.acs.org/10.1021/acsomega.2c03170

Notes

The authors declare no competing financial interest.

https://doi.org/10.1021/acsomega.2c03170
ACS Omega 2022, 7, 27587−27601

■ ACKNOWLEDGMENTS

Authors thank the center of excellence for economical production of nanomaterials (31305), PSAS, Beni-Suef University, for partial support of this work.

■ REFERENCES

(1) Hu, W.; Li, L.; Li, G.; Meng, J.; Tong, W. Synthesis of titanate-based nanotubes for one-dimensionally confined electrical properties. *J. Phys. Chem. C* **2009**, *113*, 16996−17001.
(2) Wang, X.; Liu, L. H.; Ramström, O.; Yan, M. Engineering Nanomaterial Surfaces for Biomedical Applications. *Exp. Biol. Med.* **2009**, *234*, 1128−1139.
(3) Yin, B.; Qu, S. Origin of the vanishing critical thickness for ferroelectricity in free-standing PbTiO 3 ultrathin films from first principles. *J. Appl. Phys.* **2013**, *114*, 063703.
(4) Alexe, M.; Hesse, D.; Schmidt, V.; Senz, S.; Fan, H. J.; Zacharias, M.; et al. Ferroelectric nanotubes fabricated using nanowires as positive templates. *Appl. Phys. Lett.* **2006**, *89*, 172907.
(5) Yadlovker, D.; Berger, S. Uniform orientation and size of ferroelectric domains. *Phys. Rev. B: Condens. Matter Mater. Phys.* **2005**, *71*, 184112.
(6) Luo, Y.; Szafraniak, I.; Zakharov, N. D.; Nagarajan, V.; Steinhart, M.; Wehrspohn, R. B.; et al. Nanoshell tubes of ferroelectric lead zirconate titanate and barium titanate. *Appl. Phys. Lett.* **2003**, *83*, 440−442.
(7) Morrison, FD.; Ramsay, L.; Scott, J. F. High aspect ratio piezoelectric strontium−bismuth−tantalate nanotubes. *J. Phys.: Condens. Matter* **2003**, *15*, L527−L532.
(8) Morozovska, AN.; Glinchuk, MD.; Eliseev, E. A. Ferroelectricity enhancement in ferroelectric nanotubes. *Phase Transitions* **2007**, *80*, 71−77.
(9) Maeder, M. D.; Damjanovic, D.; Setter, N. Lead Free Piezoelectric Materials. *J. Electroceram.* **2004**, *13*, 385−392.
(10) Li, B. W.; Osada, M.; Ozawa, T. C.; Sasaki, T. $RbBiNb_2O_7$: A New Lead-Free High- T c Ferroelectric. *Chem. Mater.* **2012**, *24*, 3111−3113.
(11) Zaki, A. H.; Abdel Hafiez, M.; El Rouby, W. M. A.; El-Dek, S. I.; Farghali, A. A. Novel magnetic standpoints in Na2Ti3O7 nanotubes. *J. Magn. Magn. Mater.* **2019**, *476*, 207−212.
(12) Yanagisawa, M.; Uchida, S.; Sato, T. Synthesis and photo-chemical properties of Cu^{2+} doped layered hydrogen titanate. *Int. J. Inorg. Mater.* **2000**, *2*, 339−346.
(13) Pal, D.; Abdi, SH.; Tripathi, G.; Maurya, V. K.; Khan, S. A.; Yadav, J. K.; et al. Epr And Mixed Ionic-Electronic Conductivity Studies Of Pure And Copper Doped Layered Lithium Sodium Titanate $(LiNa)Ti_3O_7$. *Int. J. Mod. Phys.: Conf. Ser.* **2013**, *22*, 374−379.
(14) Li, J.; Wan, W.; Zhu, F.; Li, Q.; Zhou, H.; Li, J.; et al. Nanotube-based hierarchical titanate microspheres: an improved anode structure for Li-ion batteries. *Chem. Commun.* **2012**, *48*, 389−391.
(15) Prodromakis, T.; Papavassiliou, C. Engineering the Maxwell−Wagner polarization effect. *Appl. Surf. Sci.* **2009**, *255*, 6989−6994.
(16) Zaki, A. H.; Naeim, A. A.; EL-Dek, S. I. Sodium titanate nanotubes for efficient transesterification of oils into biodiesel. *Environ. Sci. Pollut. Res.* **2019**, *26*, 36388−36400.
(17) Zaki, A. H.; Lee, M. J. Effects of K^{+}, Mg^{2+}, Ca^{2+}, Zn^{2+}, La^{3+}, Cr^{3+}, Ce^{3+}, Ce^{4+}, and Mo^{5+} Doping on the Adsorption Performance and Optical Properties of Sodium Titanate Nanotubes. *ACS Omega* **2019**, *4*, 19623−19634.
(18) Mansour, S. F.; Ahmed, M. A.; El-Dek, S. I.; Abdo, M. A.; Kora, H. H. Enhancement of the physical properties of novel (1−x) NiFe2O4 + (x) Al2O3 nanocomposite. *Appl. Phys.* **2017**, *123*, 480.
(19) Clark, S. J.; Segall, M. D. S.; Pickard, C. J. P.; Hasnip, P. J. H.; Probert, M. I. J. P.; Payne, K.; Payne, M. C.; et al. First principles methods using CASTEP. *Zeitschrift fur Krist* **2005**, *220*, 567−570.
(20) Kohn, W.; Sham, L. J. Self-Consistent Equations Including Exchange and Correlation Effects. *Phys. Rev.* **1965**, *140*, A1133−A1138.
(21) Zhang, Y.; Yang, W. Comment on "generalized gradient approximation made simple". *Phys. Rev. Lett.* **1998**, *80*, 890.
(22) Perdew, J. P.; Burke, K.; Ernzerhof, M. Perdew, Burke, and Ernzerhof Reply: *Phys. Rev. Lett.* **1998**, *80*, 891.
(23) Perdew, J. P.; Burke, K.; Ernzerhof, M. PerdewBurke Ernzerhof - 1997 - Generalized Gradient Approximation Made Simple. *Phys. Rev. Lett.* **1996**, *77*, 3865−3868.
(24) Perdew, J. P. *Electronic Structure of Solids*; Ziesche, P., Eschrig, H., Eds.; Akademie Verlag: Berlin, 1991; Vol. *11*.
(25) Perdew, J. P.; Ruzsinszky, A.; Csonka, G. I.; Vydrov, O. A.; Scuseria, G. E.; Constantin, L. A.; et al. Restoring the density-gradient expansion for exchange in solids and surfaces. *Phys. Rev. Lett.* **2007**, *13*, 136406.
(26) Wu, Z.; Cohen, R. E. More accurate generalized gradient approximation for solids. *Phys. Rev. B: Condens. Matter Mater. Phys.* **2006**, *73*, 235116.
(27) Dudarev, S. L.; Botton, G. A.; Savrasov, S. Y.; Humphreys, C. J.; Sutton, A. P. Electron-energy-loss spectra and the structural stability of nickel oxide: An LSDA+U study. *Phys. Rev. B: Condens. Matter Mater. Phys.* **1998**, *57*, 1505−1509.
(28) Méndez-Galván, M.; Celaya, C. A.; Jaramillo-Quintero, O. A.; Muñiz, J.; Díaz, G.; Lara-García, H. A. Tuning the band gap of M-doped titanate nanotubes (M = Fe, Co, Ni, and Cu): an experimental and theoretical study. *Nanoscale Adv.* **2021**, *3.5*, 1382−1391.
(29) Shannon, R. D.; Prewitt, C. T. Revised values of effective ionic radii. *Acta Crystallogr., Sect. B: Struct. Crystallogr. Cryst. Chem.* **1970**, *26*, 1046−1048.
(30) Mozia, S.; Borowiak-Paleń, E.; Przepiórski, J.; Grzmil, B.; Tsumura, T.; Toyoda, M.; et al. Physico-chemical properties and possible photocatalytic applications of titanate nanotubes synthesized via hydrothermal method. *J. Phys. Chem. Solids* **2010**, *71*, 263−272.
(31) Morgado, E.; de Abreu, M. AS.; Moure, G. T.; Marinkovic, B. A.; Jardim, P. M.; Araujo, A. S. Characterization of Nanostructured Titanates Obtained by Alkali Treatment of TiO^{2-}Anatases with Distinct Crystal Sizes. *Chem. Mater.* **2007**, *19*, 665−676.
(32) Thorne, A.; Kruth, A.; Tunstall, D.; Irvine, J. TS.; Zhou, W. Formation, Structure, and Stability of Titanate Nanotubes and Their Proton Conductivity. *J. Phys. Chem. B* **2005**, *109*, 5439−5444.
(33) Turki, A.; Kochkar, H.; Guillard, C.; Berhault, G.; Ghorbel, A. Effect of Na content and thermal treatment of titanate nanotubes on the photocatalytic degradation of formic acid. *Appl. Catal., B* **2013**, *138-139*, 401−415.
(34) Ahmed, M. A.; Bishay, S. T.; Abdelatif, G. Effect of ytterbium on the electrical properties of Li-Co ferrite. *J. Phys. Chem. Solids* **2001**, *62*, 1039−1046.
(35) Mansour, S. F.; Abdo, M. A.; Kzar, F. L. Effect of Cr dopant on the structural, magnetic and dielectric properties of Cu-Zn nano-ferrites. *J. Magn. Magn. Mater.* **2018**, *465*, 176−185.
(36) Mansour, S. F.; Dawood, A.; Abdo, M. A. Enhanced magnetic and dielectric properties of doped Co−Zn ferrite nanoparticles by virtue of Cr^{3+} role. *J. Mater. Sci.: Mater. Electron.* **2019**, *30*, 17262−17275.
(37) Choudhary, P.; Varshney, D. Dielectric relaxation behavior and impedance studies of Cu^{2+} ion doped Mg − Zn spinel nanoferrites. *Solid State Commun.* **2018**, *271*, 89−96.
(38) Shripal; Maurya, D.; Shalini; Kumar, J. Dielectric−spectro-scopic and AC conductivity studies in iron doped layered $Na_2Ti_3O_7$ ceramics. *Mater. Sci. Eng. B* **2007**, *136*, 5−10.
(39) Pal, D.; Abdi, S. H.; Tripathi, G.; Maurya, V. K.; Sachan, K.; Khan, S. A. Effect of heavy mixing lithium with doping of manganese on structural, EPR and dielectric spectroscopic properties of Layered $Na_2Ti_3O_7$. *J. Mater. Sci.: Mater. Electron.* **2013**, *24*, 1562−1568.
(40) Pal, D.; Pal, R. K.; Pandey, J. L.; Abdi, S. H.; Agnihotri, A. K. Bulk ac conductivity studies of lithium substituted layered sodium trititanates $(Na_2Ti_3O_7)$. *J. Mater. Sci.: Mater. Electron.* **2010**, *21*, 1181−1185.

https://doi.org/10.1021/acsomega.2c03170
ACS Omega 2022, 7, 27587−27601

(41) Riess, I. The possible use of mixed ionic electronic conductors instead of electrolytes in fuel cells. *Solid State Ionics* **1992**, *52*, 127−134.
(42) Ivanova, S.; Penkova, A.; Hidalgo, M. D. C.; Navío, J. A.; Romero-Sarria, F.; Centeno, M.; et al. Synthesis and application of layered titanates in the photocatalytic degradation of phenol. *Appl. Catal., B* **2015**, *163*, 23−29.
(43) El Rouby, W. M. A. Selective adsorption and degradation of organic pollutants over Au decorated Co doped titanate nanotubes under simulated solar light irradiation. *J. Taiwan Inst. Chem. Eng.* **2018**, *88*, 201−214.
(44) Catlow, C. R. A.; Cormack, A. N.; Théobald, F. Structure prediction of transition-metal oxides using energy-minimization techniques. *Acta Crystallogr. Sect. B Struct. Sci.* **1984**, *40*, 195−200.

https://doi.org/10.1021/acsomega.2c03170
ACS Omega 2022, 7, 27587−27601